Supporting information for "Trace elements in PM$_{2.5}$ aerosols in East Asian outflow in the spring of 2018; Emission, transport, and source apportionment"

Takuma Miyakawa[1], Akinori Ito[1], Chunmao Zhu[1], Atsushi Shimizu[2], Erika Matsumoto[3], Yusuke Mizuno[3], Yugo Kanaya[1]

[1]Research Institute for Global Change, Japan Agency for Marine-Earth Science and Technology, Yokohama, 236-0001, Japan

[2]Regional Environment Conservation Division, National Institute for Environmental Studies, Tsukuba, 305-8506, Japan

[3]Horiba Ltd., Ohtsu, 520-0102, Japan

Correspondence to: Takuma Miyakawa (miyakawat@jamstec.go.jp)

This supporting information includes details of the multiple linear regression (MLR) model and 11 figures and 1 table.

S1. Source apportionment of PM$_{2.5}$ aerosols based on multilinear regression (MLR) analyses

In Sect. 3.5.1, MLR model was applied to the source apportionment of PM$_{2.5}$ aerosols using the temporal variations in concentrations of silica, black carbon, and sulfate ($[Si]_t$, $[BC]_t$, and $[SO_4^{2-}]_t$, respectively). Before determining the input variables for this analysis, several cases were tested based on the following equations:

$$[PM_{2.5}]_t = g_{Si} \cdot [Si]_t + g_{sulfate} \cdot [SO_4^{2-}]_t + C1 \qquad \text{(Eq. S1)}$$

$$[PM_{2.5}]_t = g_{BC} \cdot [BC]_t + g_{Si} \cdot [Si]_t + C2 \qquad \text{(Eq. S2)}$$

$$[PM_{2.5}]_t = g_{BC} \cdot [BC]_t + g_{Si} \cdot [Si]_t + g_{sulfate} \cdot [SO_4^{2-}]_t + C3 \qquad \text{(Eq. S3)}$$

The coefficients g_X (X = BC, Si, and sulfate) and C1–C3 (i.e., the constant term for the Eqs. (S1)–(S3)) were determined by the least squares method. The fitting residuals (i.e., chi square) for these cases were analyzed to diagnose the impacts of the input variables on the MLR model's performance. The values of chi square for the Eqs. (S1)–(S3) were determined to be 13936.2, 10166.6, and 8337.6, respectively. Putting these three components in the MLR model led to the minimum values of chi-square among these three cases. The comparison of the results between Eqs. (S1) and (S2) suggested that [BC] and [Si] can better account for $[PM_{2.5}]_t$ than $[SO_4^{2-}]_t$ and $[Si]_t$, indicating that $[BC]_t$ can be a tracer for not only primary anthropogenic emissions but also a part of secondary formation from the anthropogenic sources in this study. This was expected from the observed positive correlation between $[BC]_t$ and $[SO_4^{2-}]_t$ (**Figure S7**). As the value of $g_{sulfate}$ for Eq. (S3) was less than unity, the SO$_4^{2-}$ related component cannot represent all the variations in the impacts of the secondary formations of inorganic (e.g., ammonium sulfate and nitrate) and organic aerosols (OAs). Thus, SO$_4^{2-}$ related components can represent the aqueous phase production reaction of SO$_4^{2-}$ and OAs in aerosol and cloud droplet phases. The value of C3 (4.95 μg m^{-3}) represents the background levels of $[PM_{2.5}]_t$ in East Asian outflow in the spring of 2018 and can include the sea salt (SS) aerosols emitted

from the ocean surface and some other secondary aerosols. In this study, the impacts of SS aerosols on the source apportionment of $PM_{2.5}$ aerosols were assessed using the temporal variations of chlorine concentrations $[Cl]_t$ in $PM_{2.5}$ aerosols, which were measured using the PX-375. As SS aerosols are chemically reactive and chlorine in SS can be removed by the reaction with acidic gases such as sulfuric acid, SS mass concentrations from the $[Cl]_t$ with the assumed seawater composition can be estimated as its lower estimate ($[SS_{MIN}]_t$). The SS_{MIN} contributed approximately 13% of $PM_{2.5}$ aerosol mass on average during the study period and was lower than C3, indicating that SS can account for almost half of the background level of $[PM_{2.5}]_t$ during the study period. The source apportionment of non-sea-salt components of $PM_{2.5}$ aerosols (nss-$PM_{2.5}$) was also analyzed in the same manner as follows:

$$[\text{nss-}PM_{2.5}]_t = [PM_{2.5}]_t - [SS_{MIN}]_t = g_{BC} \cdot [BC]_t + g_{Si} \cdot [Si]_t + g_{sulfate} \cdot [SO_4^{2-}]_t + C4 \qquad \text{(Eq. S4)}$$

The results for fitting the MLR models to the observed $PM_{2.5}$ and nss-$PM_{2.5}$ aerosols are summarized in Table S1. The sum of C4 and the average values of $[SS_{MIN}]_t$ (4.69 µg m^{-3}) were almost the same as C3, indicating that SS components had no substantial impacts on the source apportionment using Eq. (S3). Indeed, the changes in the contributions of dust to total $PM_{2.5}$ aerosols ($g_{Si} \cdot [Si]_t/[PM_{2.5}]_t$) among Eqs. 3 and 4 were small (only 4% differences). As Cl is not a perfectly adequate tracer for SS aerosols, we selected Eq. 3 for the base case calculations of the source apportionments of $PM_{2.5}$ aerosols.

Table S1. Results of the MLR analyses for the $PM_{2.5}$ aerosols using Eqs. (S3) and (S4)

Eqs.	Chi-square	g_{Si}	g_{BC}	$g_{sulfate}$	C3 or C4
S3	8337.6	4.62 (±0.29)	20.78 (±2.15)	0.66 (±0.12)	4.95 (±0.60)
S4	9021.7	4.79 (±0.30)	23.45 (±2.23)	0.56 (±0.12)	2.26 (±0.63)

*Values in the parentheses are 95% confidence interval for the determined coefficients.

The source apportionment results using Eq. (S3) were compared with those simulated by the IMPACT model (Ito and Miyakawa, 2023). **Figure S8** depicts the temporal variations of the observed, estimated, and modeled mass concentrations of $PM_{2.5}$ total, dust, non-dust (i.e., anthropogenic and secondary formation), and SS aerosols. The mass concentrations of the observed $PM_{2.5}$ total and the estimated dust and non-dust aerosols agreed well with those simulated by the IMPACT model, indicating that the dust fraction of $PM_{2.5}$ aerosols was successfully classified using Si as a tracer of dust aerosols. The SS_{MIN} showed similar concentration levels to the SS model; however, the temporal variations of the SS_{MIN} were not well reproduced by the IMPACT model. This is likely because the sub-grid scale sea spraying affecting the observed SS concentrations cannot be well simulated by the IMPACT model, whose horizontal resolution was 2.0° × 2.5° (latitude × longitude). The average levels of SS_{MIN} (2.43±2.11 µg m^{-3}) and SS modeled (2.24±2.01 µg m^{-3}) were lower than C3. The difference can be accounted for by the other components, such as sulfate and secondary organic aerosols, which can be regionally homogeneous in the springtime East Asian outflow (e.g., Matsui et al., 2014).
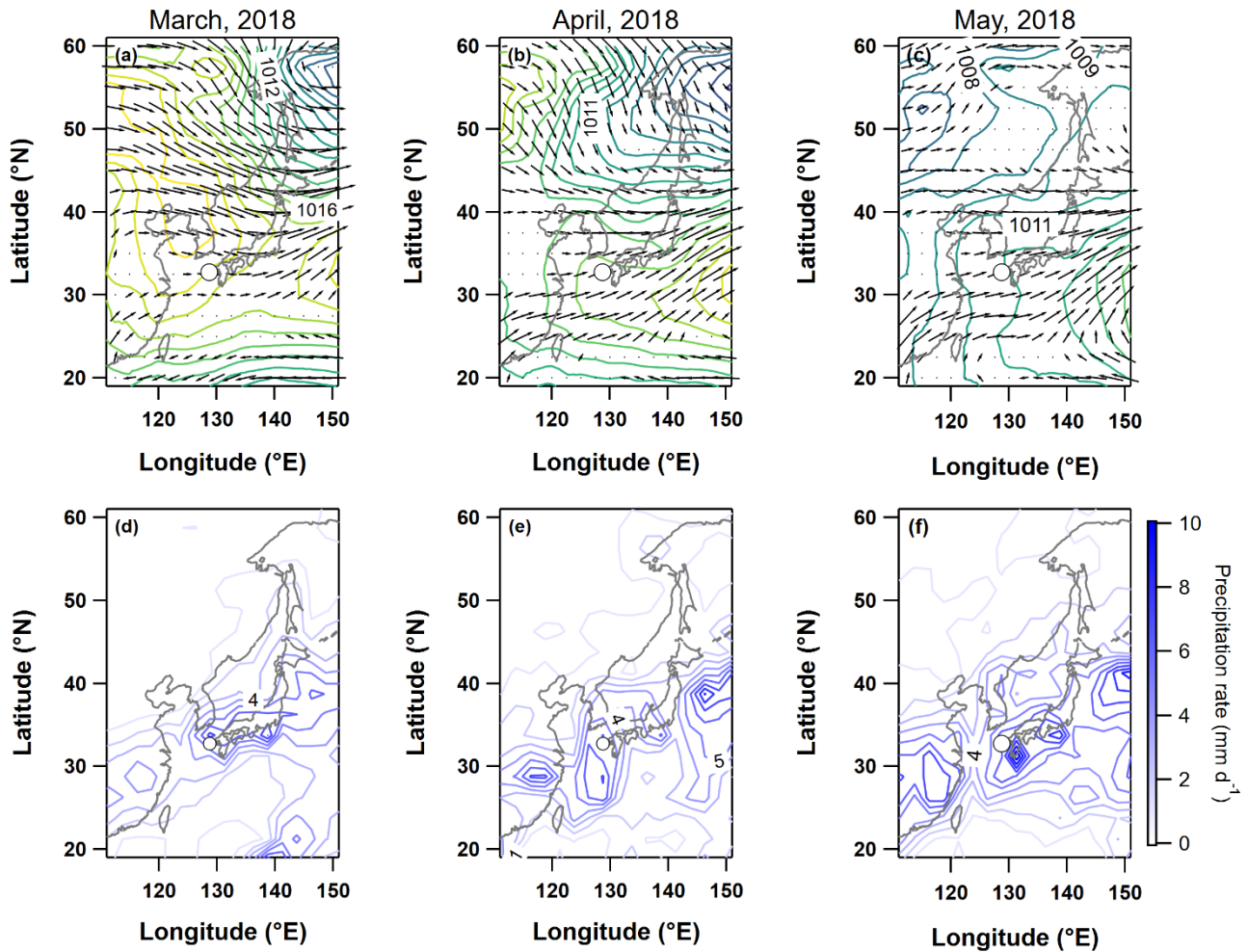
65 **Figure S1.** Monthly mean sea level pressure as contours and wind vectors at 850 hPa for (a) March, (b) April, and (c) May of 2018. Monthly mean precipitation rate for (d) March, (e) April, and (f) May of 2018. Monthly mean meteorological and precipitation data with a resolution of 1° in latitude and longitude were obtained from the National Centers for Environmental Prediction (NCEP) reanalysis and the Global Precipitation Climatology Project (GPCP), respectively.

70
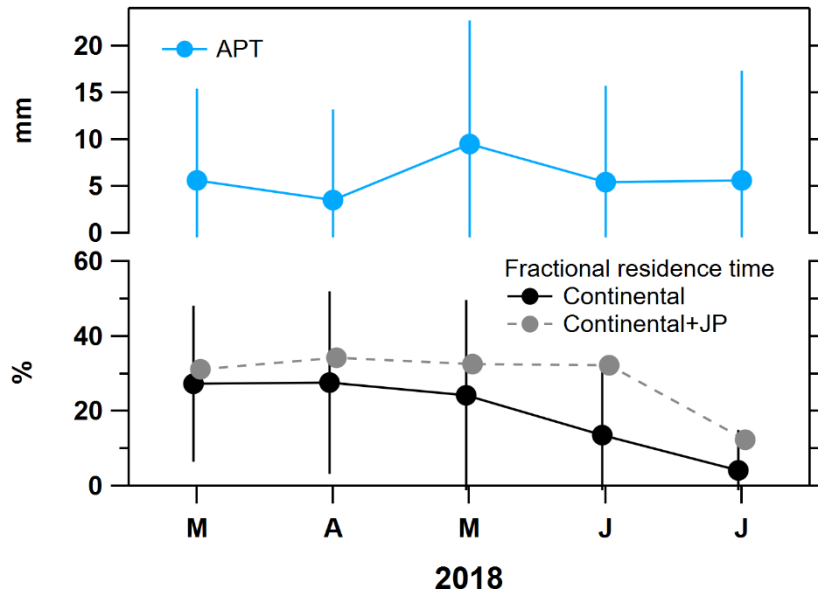
Figure S2. Seasonal progression of the monthly mean accumulated precipitation along trajectories (light blue markers and lines) in the top panel and the monthly mean fractional residence time over the continents (black markers and lines) and Japan (shaded markers and dashed lines) in the bottom panel. All the vertical bars represent the standard deviations of the monthly mean.
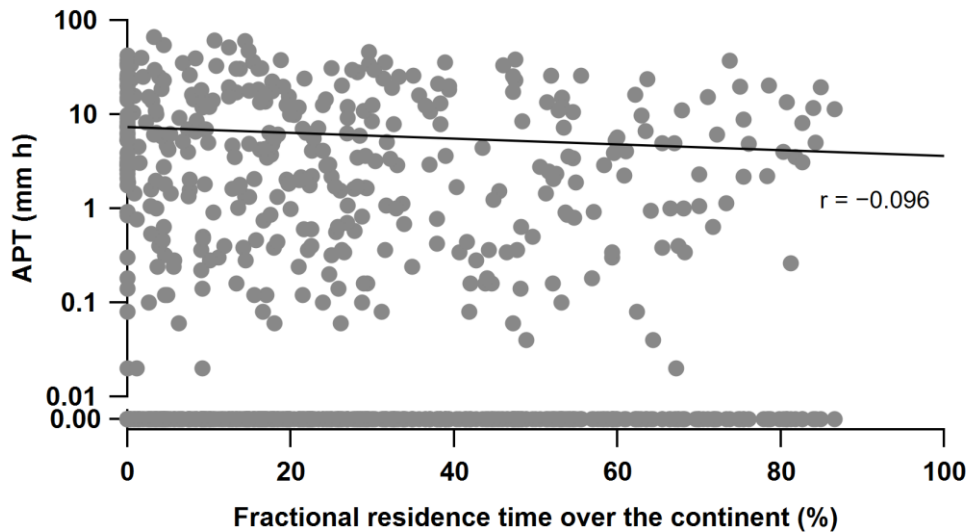
Figure S3. Relationship between the accumulated precipitation along trajectories and fractional residence time over the continent. The solid line depicts the linear regression line, which indicates that no significant correlation exists between the two parameters.
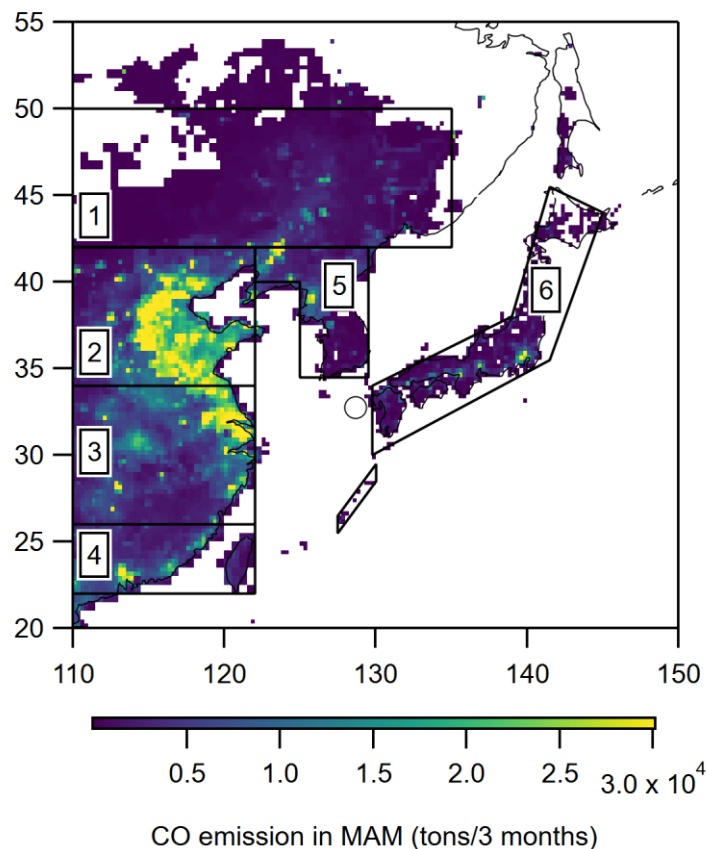
Figure S4. Anthropogenic carbon monoxide (CO) emission in the springtime (March–May, 2008) at East Asia from Regional Emission inventory in ASia (REAS v2.1) (Kurokawa et al., 2013). The encircled and labeled areas are considered for the calculations of fractional residence time (1: northeast China; 2: north central China; 3: south central China; 4 south China; 5: Korea; and 6: Japan). The East Asian continent is defined as the area labeled as 1–5.
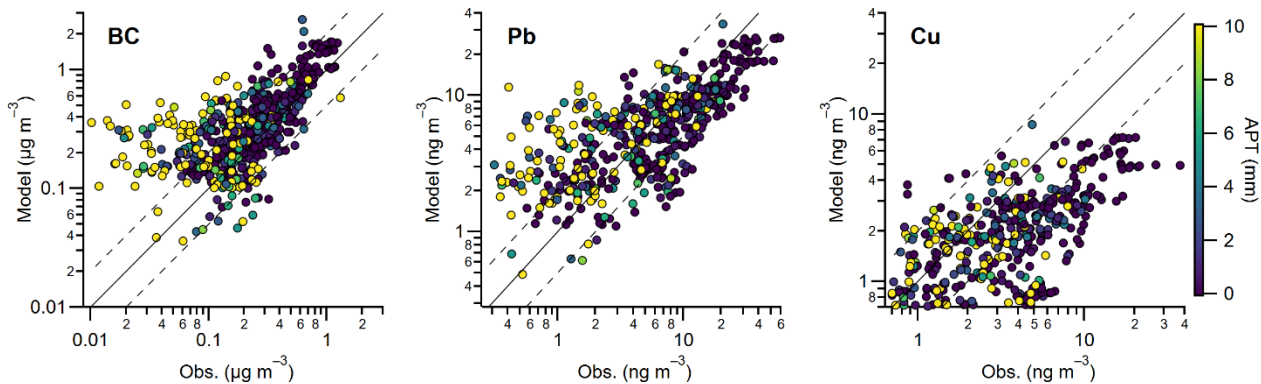
Figure S5. Correlations between the modeled and observed concentrations of black carbon (BC) (left), Pb (middle), and Cu (right) are colored by the values of the accumulated precipitation along trajectories. The solid line indicates the 1:1 line, and the two dashed lines indicate the boundaries of the factor of 2.
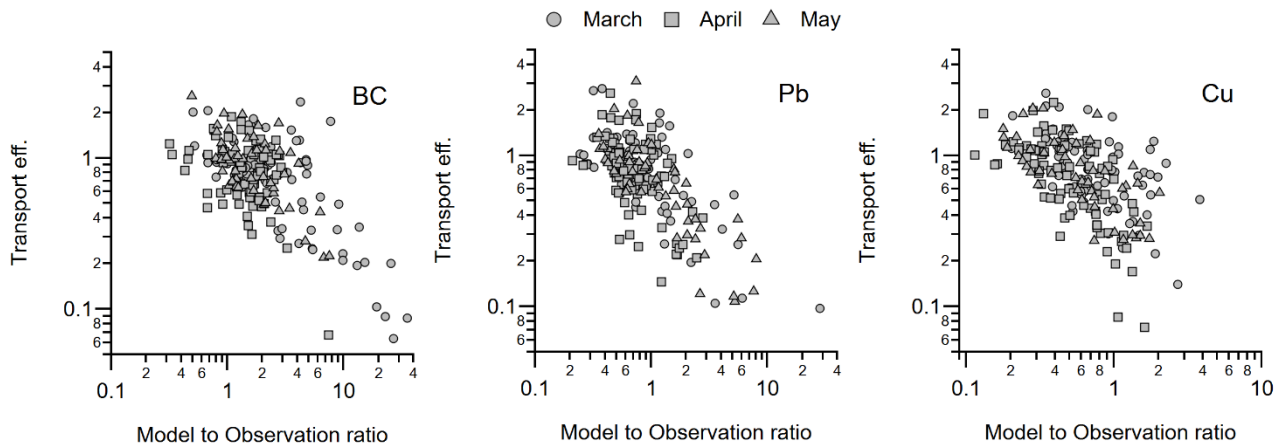
Figure S6. Relationship between transport efficiency and model-to-observation ratios for black carbon (BC) (left), Pb (middle), and Cu (right). Shaded markers for 4-hourly data points are differentiated by the month (circles (March); squares (April); triangles (May)) of 2018.
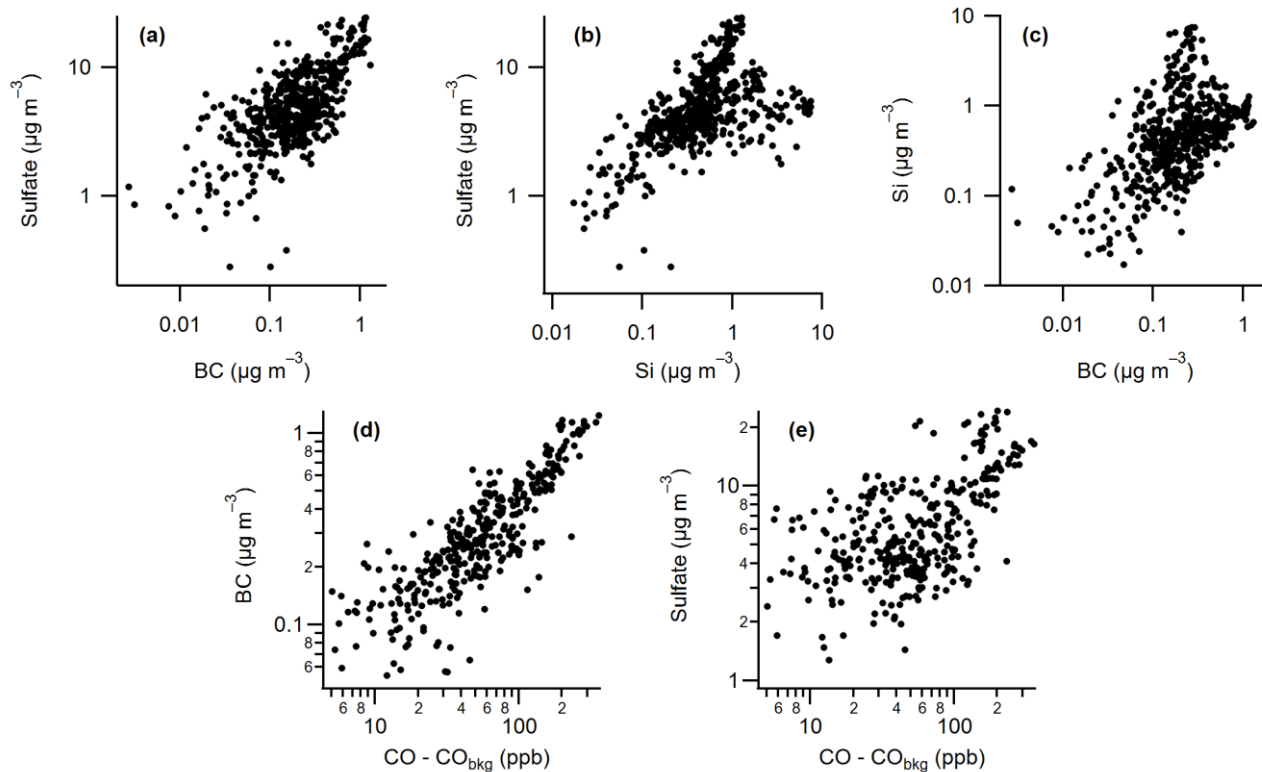
Figure S7. Correlations of (a) black carbon (BC) and sulfate concentrations, (b) Si and sulfate concentrations, (c) BC and Si concentrations, (d) the enhancements of carbon monoxide (CO) from the background (ΔCO, see the main texts for the details) and BC concentrations, and (e) ΔCO and sulfate concentrations.

100
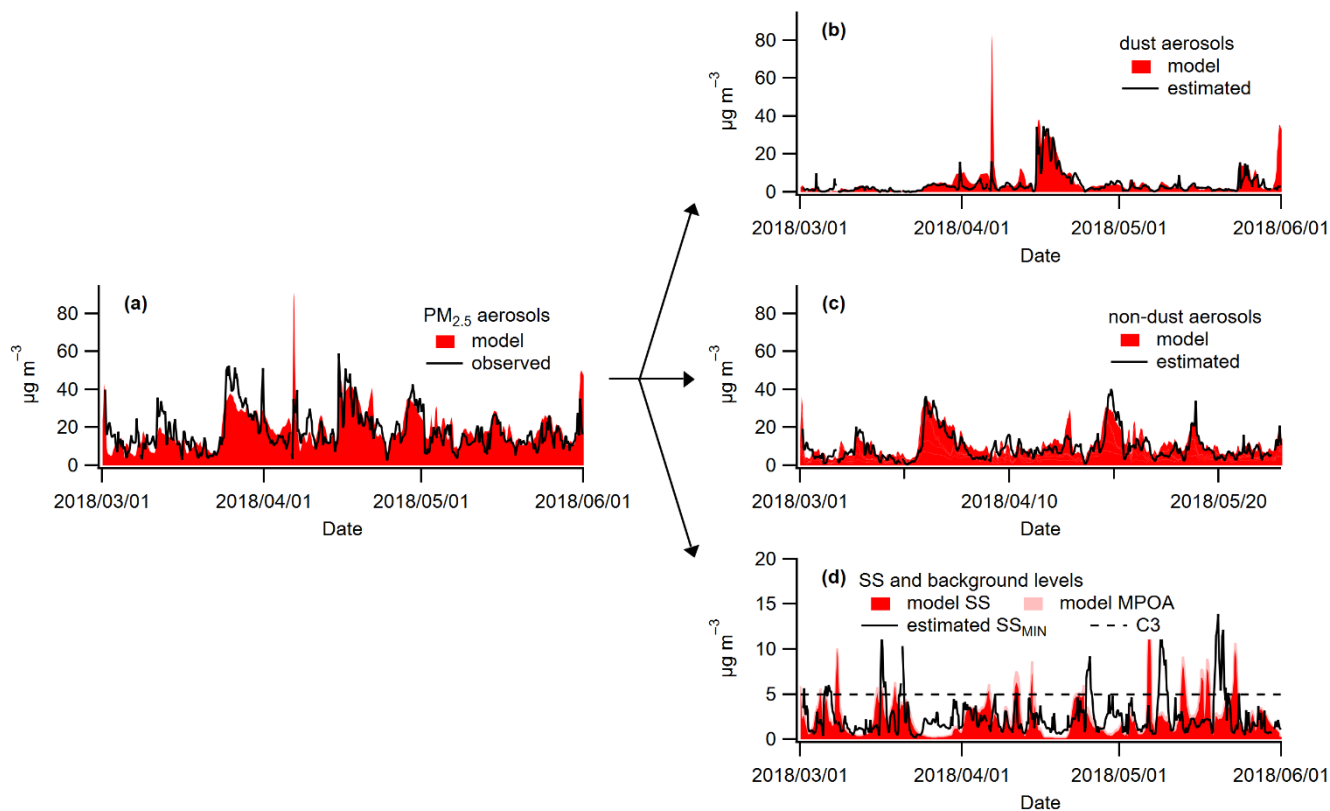
Figure S8. (a) Temporal variations in the modeled (red-filled area) and observed (black line) PM$_{2.5}$ aerosol concentrations. The temporal variations in the modeled (red-filled area) and estimated (black line) PM$_{2.5}$ dust (b) and non-dust (c) aerosol concentrations. The estimation was based on the equation S3 in Sect. S1 of this supporting information. (d) The temporal variations in the modeled (red-filled area) and estimated (black line) PM$_{2.5}$ sea salt (SS) concentrations. The modeled marine primary organic aerosol (MPOA, light red area) was stacked on the modeled SS in (d). The coefficient C3 in the MLR model using the equation S3 was also overlayed as the dashed line in (d).
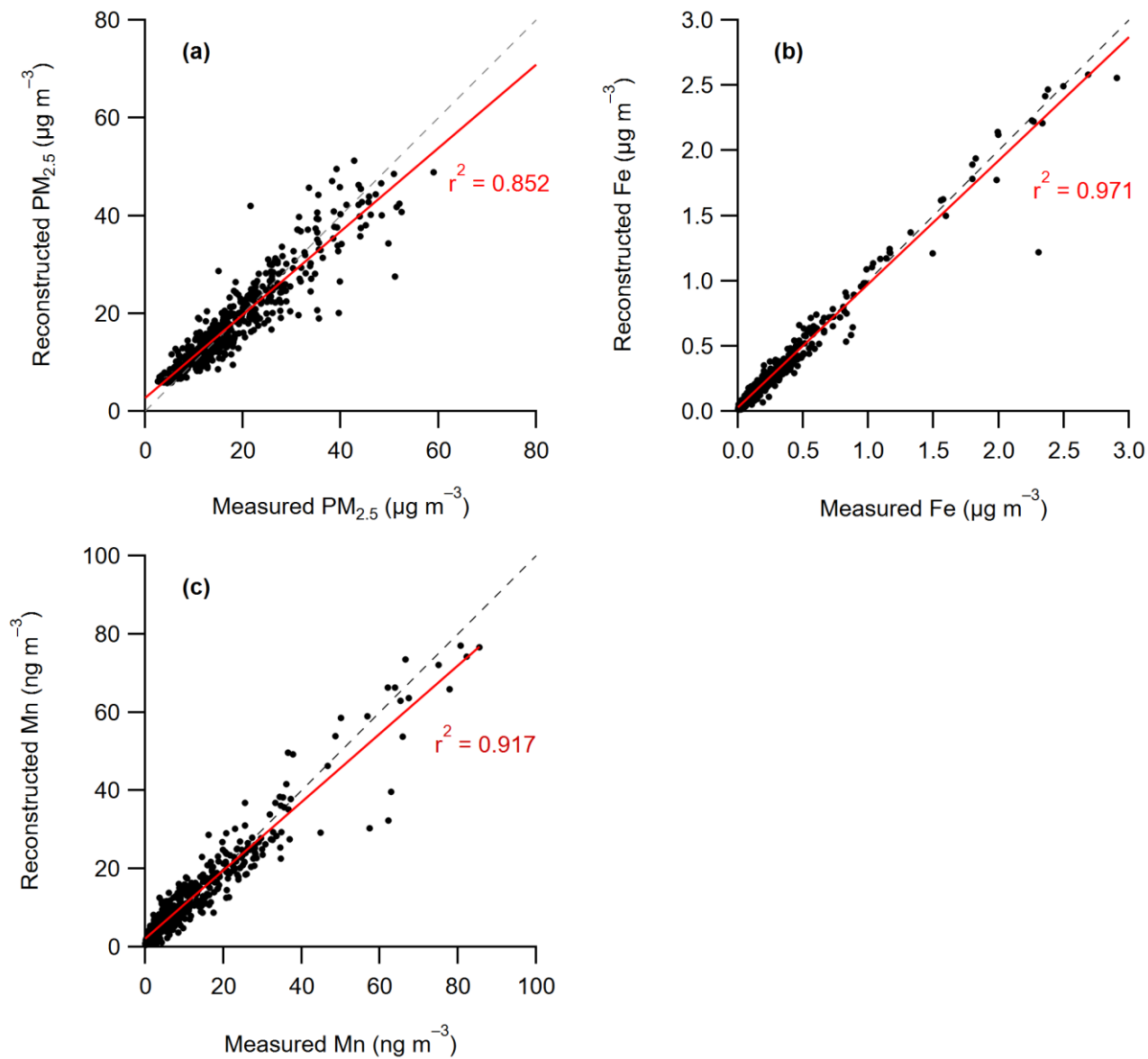
110

Figure S9. Correlations between the reconstructed and measured concentrations for (a) total PM$_{2.5}$ aerosols, (b) PM$_{2.5}$ Fe aerosols, and (c) PM$_{2.5}$ Mn aerosols. The dashed lines depict the 1:1 line, and red lines depict the linear regression lines for the correlations.
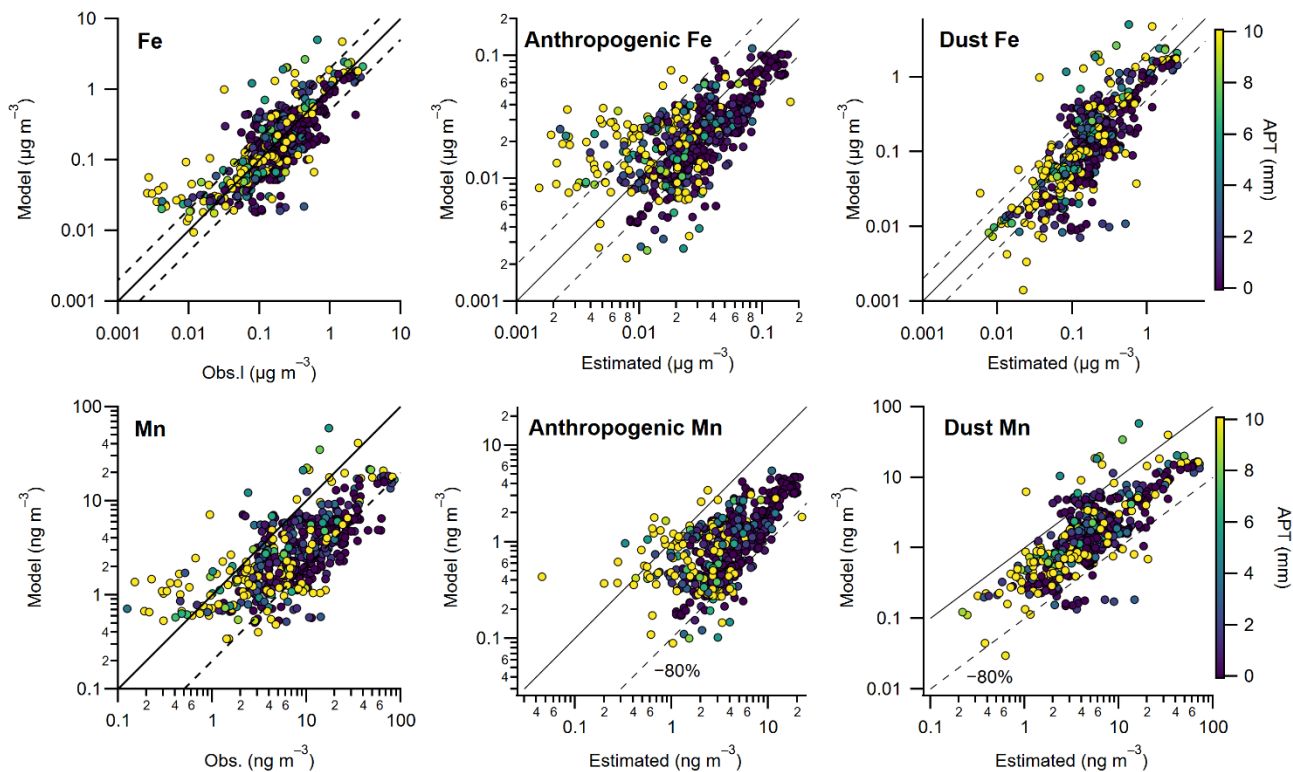
Figure S10. (Top) Correlations of the modeled and observed/estimated concentrations of (left) total-Fe, (middle) anthropogenic-Fe, and (right) dust-Fe. (bottom) Correlations of the modeled and observed/estimated concentrations of (left) total-Mn, (middle) anthropogenic-Mn, and (right) dust-Mn. All the data points are colored by the values of the accumulated precipitation along trajectories (APT). The black line depicts the 1:1 line. The dashed two lines in the top panel depict the boundaries of the factor 2. The dashed line in the bottom panel depicts the -80% of the model-to-estimation ratios.

115

120
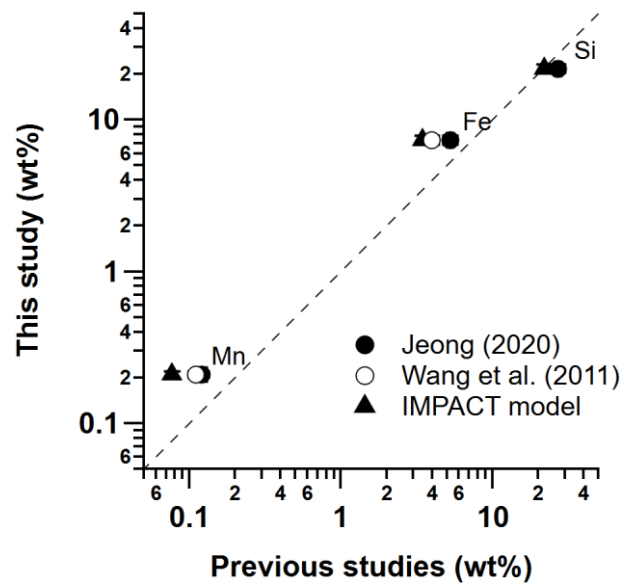
Figure S11. Comparison of the dust elemental compositions between this study and the other studies (filled circles: Jeong, 2020; open circles: Wang et al., 2011; triangles: modeled given in Ito and Miyakawa, 2023). The dashed line represents the 1:1 line.

References

Ito, A., and Miyakawa, T.: Aerosol iron from metal production as a secondary source of bioaccessible iron. Environ. Sci. & Tech., 57(10), 4091–4100, https://doi.org/10.1021/acs.est.2c06472, 2023.

Jeong, G. Y.: Mineralogy and geochemistry of Asian dust: dependence on migration path, fractionation, and reactions with polluted air, Atmos. Chem. Phys., 20, 7411–7428, https://doi.org/10.5194/acp-20-7411-2020, 2020.

Kurokawa, J., Ohara, T., Morikawa, T., Hanayama, S., Janssens-Maenhout, G., Fukui, T., Kawashima, K., and Akimoto, H.: Emissions of air pollutants and greenhouse gases over Asian regions during 2000?2008: Regional Emission inventory in ASia (REAS) version 2, Atmos. Chem. Phys., 13, 11019–11058, https://doi.org/10.5194/acp-13-11019-2013, 2013.

Matsui, H., Koike, M., Kondo, Y., Takami, A., Fast, J. D., Kanaya, Y., and Takigawa, M.: Volatility basis-set approach simulation of organic aerosol formation in East Asia: implications for anthropogenic biogenic interaction and controllable amounts, Atmos. Chem. Phys., 14, 9513–9535, https://doi.org/10.5194/acp-14-9513-2014, 2014.

Wang, Q., Zhuang, G., Li, J., Huang, K., Zhang, R., Jiang, Y., Lin, Y., and Fu, J. S.: Mixing of dust with pollution on the transport path of Asian dust – revealed from the aerosol over Yulin, the north edge of Loess Plateau. Sci. Tot. Environ., 409(3), 573–581, https://doi.org/10.1016/j.scitotenv.2010.10.032, 2011.